POLITECNICO DI TORINO
Repository ISTITUZIONALE

A NON-LOCAL KINETIC MODEL FOR CELL MIGRATION: A STUDY OF THE INTERPLAY BETWEEN CONTACT GUIDANCE AND STERIC HINDRANCE

(Article begins on next page)

11 July 2024

A NON-LOCAL KINETIC MODEL FOR CELL MIGRATION: A STUDY OF THE INTERPLAY BETWEEN CONTACT GUIDANCE AND STERIC HINDRANCE*

MARTINA CONTE† AND NADIA LOY†

Abstract. We propose a non-local model for contact guidance and steric hindrance depending on a single external cue, namely the extracellular matrix, that affects in a twofold way the polarization and speed of motion of the cells. We start from a microscopic description of the stochastic processes underlying the cell re-orientation mechanism related to the change of cell speed and direction. Then, we formally derive the corresponding kinetic model that implements exactly the prescribed microscopic dynamics, and, from it, it is possible to deduce the macroscopic limit in the appropriate regime. Moreover, we test our model in several scenarios. In particular, we numerically investigate the minimal microscopic mechanisms that are necessary to reproduce cell dynamics by comparing the outcomes of our model with some experimental results related to breast cancer cell migration. This allows us to validate the proposed modeling approach and to highlight its capability of predicting qualitative cell behaviors in diverse heterogeneous microenvironments.

Key words. non-local model, kinetic transport equations, Markovian processes, contact guidance, steric hindrance, extracellular matrix

MSC codes. 92B05, 92C17, 60J05, 35Q20

DOI. 10.1137/22M1506389

1. Introduction. It is well established that cell migration, based on diverse migration modes, is essential for normal processes such as embryonic development, immune function, and tissue repair and that it also plays a critical role in disease states, including cancer dissemination [29, 38, 39, 40, 42, 43]. The process of cell migration is greatly affected by the surrounding microenvironment that cells sense through their protrusions and to which they respond by adapting their dynamics. A prominent role in cell migration is played by the extracellular matrix (ECM), that is the fiber-like component present within all tissues and organs which provides physical scaffolding for the cellular constituents. One of the major ECM components is collagen, which represents up to 30% of the total protein mass of a multicellular animal and, in particular, type I collagen is the most abundant one in the human body [4].

The influence of the ECM on cell migration. There are several biophysical and biochemical factors of the ECM, in particular of collagen, that influence cell migration. The ones having a major impact are related to confinement, rigidity, topology, and adhesion properties [4]. Each one of these features gives rise to certain cell migration responses, and it is often difficult from the experimental point of view to decouple the different aspects in order to investigate the effect and role of each of them separately. However, understanding every single mechanism and its specific role in the overall

---

†Department of Mathematical Sciences "G. L. Lagrange," Politecnico di Torino, 10129 Torino, Italy (martina.conte@polito.it, nadia.loy@polito.it).

dynamics is important for extrapolating in vitro analyses to in vivo situations. For instance, one of the most outstanding goals in the context of cancer spread and dissemination is the development of therapeutic strategies targeting specific mechanisms that play a crucial role in cancer cell invasion.

The ECM is characterized by a number of mechanical, biophysical, and chemical properties influencing cell migration, which is governed by the interplay between cell-generated propulsion forces, adhesion forces, and resisting forces arising from the steric hindrance properties of the matrix. It is possible to identify some factors that influence the direction of the cells and others that affect their speed. Specifically, the alignment of the collagen fibers is shown to stimulate *contact guidance* [15, 14], which is the tendency of cells to migrate by crawling on the fibers and following the directions imposed by them. Concerning the speed, it generally depends on mechanical and biophysical properties of the ECM such as stiffness, porosity, and collagen density. On a flat surface, migration speed decreases with matrix stiffness mainly due to the increased stability of focal adhesions. In a three-dimensional (3D) environment, cell migration has a biphasic nature, as it is additionally impaired by the *steric hindrance* properties of the ECM that impose resisting forces to cell migration and can affect cells' motility. Steric hindrance depends on mechanical and structural matrix properties (pore size and fiber spacing, collagen density) as well as cell properties (cell size, cell stiffness) [8, 22, 52, 15, 51]. Here, we shall focus on the effect of pore size and collagen density in 3D migration. In particular, these can lead to physical limits if the pores are too narrow and, thus, represent a steric obstacle to cell motion. Conversely, if the spacing between the fibers is larger than the cell size, then cells start having difficulties in forming the adhesion contact necessary for their motility. As the pores' average size may be related to the ECM density M, cells' mean speed may be expressed as a function of M [51]. In particular, it is found that there is an optimal matrix density M_{max} ensuring the maximum possible speed and a threshold value M_{th}, which corresponds to a small pore size, that hampers the cell from moving in a certain direction [51]. Specifically, in [51], the authors show that the dependence of the speed on the ECM pore size is linear, but the dependence of the density on the pore size is not linear. Moreover, in [4], the dependence of the speed on the ECM pore size (and therefore on the ECM density) has been shown to have a parabola-like behavior, and this has been used in previous works [25]. Thus, the mean speed can be seen as a quadratic-like function of the ECM density.

Moreover, they investigate only the range of densities that are above M_{max}, i.e., the value allowing for the maximal speed, as they only consider the range of densities that if increased cause a decrease in the cell speed, while we consider a larger range of ECM densities, considering eventually vanishing ECM densities (large pore size), ECM densities (corresponding to smaller pores) that help cell motility, and very high densities (very small pores) that hinder cells from moving and constitute a physical limit of migration. In this case, it is known that the dependence of the speed on the ECM pore size (density) has a parabola-like behavior as shown in [4] and references therein. This is why this quadratic (parabola-like) behavior of the speed has also been used in previous works [24, 25].

The role of the ECM in breast cancer dissemination. Cell-ECM interactions have particular importance in the development and dissemination of breast cancer cells. In fact, the *stromal* matrix surrounding tumors may be highly linearized and this would enhance cancer invasiveness [18, 38, 42, 43]. Thus, the study of cell response to a locally aligned matrix is of utmost interest, as it could suggest therapeutic strategies to target stromal invasion. In particular, in [38], the authors introduce the concept of

tumor-associated collagen signatures (TACS) that are used to stage mammary carcinoma tumor progression levels. In [8], the authors investigate the role of steric hindrance on MDA-MB 231 breast cancer cells in 3D collagen gels, looking into the impact of stiffness and density of collagen. In particular, concerning the role of collagen density, it is known that collagen-dense breast tissue also increases the risk of breast carcinoma, although the relationship between collagen density and tumorigenesis is not well understood [40]. In [34], the authors perform experiments showing that increasing matrix density leads to reduced mean squared displacements and cell speeds (both mean and effective velocity). A first attempt to replicate these experimental results has been done in [17], where the authors propose a microscopic model in which they impose an external drag force to mimic ECM influence on cell speed. They assume that cells undergo increasing difficulty when migrating in denser, and consequently more viscous, matrices. This allows them to recover the fact that higher matrix densities imply lower speeds and mean squared displacements. Then, they impose a cubic net locomotive force with some ad hoc coefficients to recover the appropriate values of the speeds. Finally, in [44], the authors investigate through a model the role of contact guidance and steric hindrance in the presence of cyclic stress.

As a matter of fact, the interplay between contact guidance and steric hindrance plays a significant role in breast cancer progression and dissemination. Provenzano, in particular, highlights the prominent role of these two aspects in his works [38, 40]. Notwithstanding, a systematic study of the coupling of these two aspects has not been well investigated. This is mainly related to the difficulty of building experimental settings in which the two mechanisms can be studied together as purely superposing effects, for instance because the alignment of the fibers alters the porosity at the microscopic scale [49]. For the above reasons, we want to introduce a mathematical model that takes into account at the same time contact guidance and ECM porosity/density impact on the cell speed. This would allow us to perform *in silico* experiments combining these two mechanisms and make predictions on the possible way cells sort or combine the two processes. Existing models regarding cell migration on the ECM with a particular focus on the role of confinement and ECM porosity/density influence on the cell speed include individual-based models [46, 47], kinetic models [26], and mechanical models [37, 36]. On the other hand, contact guidance has also been successfully described at the mesoscopic level through kinetic equations in [10, 19], where the authors propose models that allow one to take into account the variation of the microscopic velocities in response to a given ECM fiber network. Moreover, kinetic equations have been proven to be very successful in modeling cell migration [1, 3, 5, 6, 11, 12, 19, 24, 25, 26, 27].

Kinetic models, in general, are intrinsically multiscale models. They allow one to start from the microscopic description of the dynamics, including measurable parameters of the individual migration, and to derive a mesoscopic model in which cells' position and velocity, which follow the prescribed microscopic dynamics, are statistically described by a distribution function. The time evolution of this function is ruled by a kinetic transport equation with a turning (or scattering) operator that implements the defined microscopic dynamics. By introducing the moments of the distribution function, it is also possible to derive macroscopic formulations describing the overall dynamics of the system. A particular class of kinetic equations is the one implementing *velocity-jump processes* [48]. These are microscopic Markovian processes that prescribe a *transition probability* T of choosing a new velocity and a *frequency of re-orientation* η, thus being $\frac{1}{\eta}$, the mean run time spent running on

a linear tract between two consecutive re-orientations. Such equations are popularly used to model the cell migration mode called *run and tumble,* consisting in alternating runs over straight lines and re-orientations, and they allow one to do complete statistics regarding migration quantities (mean squared displacement, mean and effective speed, etc.) [31].

In this note, we shall propose a non-local model for contact guidance and steric hindrance. As done in [25, 26], we consider different processes for the speed and polarization of a cell, but, in the present work, there is a single external cue, the ECM. The ECM is described statistically in terms of its macroscopic density and statistical distribution of the fiber direction affecting cell speed and direction, respectively. The ECM is evaluated non-locally in the physical space. The non-locality is due to the fact that cells sense the ECM and, thus, the direction of the fibers by extending their protrusions, which are a great determinant in contact guidance [2] and, in general, in the presence of strong heterogeneous or anisotropic environments [18, 38, 45]. In particular, we state a microscopic discrete in time stochastic process from which we formally derive the kinetic model. To do this, we shall take advantage of classical tools of kinetic theory, mostly used in the literature of multi-agent systems [7, 33]. Precisely, this has its roots in the classical kinetic theory for gas dynamics and describes the dynamics through microscopic *interaction rules* and *collision-like kinetic Boltzmann–Povzner equations* for non-local interactions. Such equations allow for a large variety of well-consolidated analytical tools, e.g., derivation procedures, the quasi-invariant limit, and limit scaling procedures. However, they are poorly known in the community of cell migration modeling. Thus, in section 2.1 we describe more accurately the microscopic dynamics through these interaction rules. Then, in section 2.2, after establishing a parallelism with the most known velocity jump process, we formally derive the kinetic model that exactly implements the microscopic dynamics. Moreover, in section 2.3, we briefly review some classical procedures for deriving macroscopic models in the appropriate regime on the basis of the observed experimental parameters. Finally, we test our model in several scenarios in section 3. We observe its ability to replicate different experimental results presented in [34, 50] and related to breast cancer cell migration as well as to qualitatively predict cell behavior in response to heterogeneous microenvironments.

2. Mathematical modeling. Our aim is to describe cell migration by modeling the re-orientation mechanism at the microscopic level and by means of formally derived kinetic equations. Each cell will be identified by its position $\mathbf{x} \in \Omega \subset \mathbb{R}^d$, speed $v \in [0, U]$, U being the maximum speed a cell can achieve, and polarization direction $\hat{\mathbf{v}} \in \mathbb{S}^{d-1}$, so that $\mathbf{v} = v\hat{\mathbf{v}}$, which belongs to the sphere of radius U, is the microscopic velocity vector. The distribution density function $p = p(t, \mathbf{x}, v, \hat{\mathbf{v}})$, with $t > 0$, describes the statistical distribution of the speeds and directions for cells at time t and located in $\mathbf{x}$.

Aggregate quantities, usually referred to as *macroscopic quantities,* describing the cell population, can be defined as the *statistical moments* of the distribution p, i.e.,

– the cell number (or macroscopic) density, which is the expected mass in $(t, \mathbf{x})$:

$$(2.1) \qquad \rho(t, \mathbf{x}) = \int_0^U \int_{\mathbb{S}^{d-1}} p(t, \mathbf{x}, v, \hat{\mathbf{v}}) \, d\hat{\mathbf{v}} \, dv,$$

– the mean velocity of cells located in $\mathbf{x}$ at time t:

$$(2.2) \qquad \mathbf{U}(t, \mathbf{x}) = \frac{1}{\rho(t, \mathbf{x})} \int_0^U \int_{\mathbb{S}^{d-1}} p(t, \mathbf{x}, v, \hat{\mathbf{v}}) \mathbf{v} \, d\hat{\mathbf{v}} \, dv \, .$$

We are interested in cell migration on the ECM and, in particular, in two mechanisms: *contact guidance,* which concerns the choice of the direction and depends on the fibrous structure of the ECM, and *steric hindrance,* which affects cell speed and is regulated by the density of the ECM itself. Therefore, we introduce the distribution function of the ECM fibers $m = m(\mathbf{x}, \hat{\mathbf{v}}), \hat{\mathbf{v}} \in \mathbb{S}^{d-1}$, describing the statistical distribution of the fibers identified by their direction $\hat{\mathbf{v}} \in \mathbb{S}^{d-1}$ in each point of the physical space $\mathbf{x} \in \Omega \subset \mathbb{R}^d$. As we do not consider remodeling, the distribution m is stationary. The macroscopic density of the ECM is defined at each point $\mathbf{x} \in \Omega$ by

$$(2.3) \qquad M(\mathbf{x}) := \int_{\mathbb{S}^{d-1}} m(\mathbf{x}, \hat{\mathbf{v}}) \, d\hat{\mathbf{v}}.$$

Hence, the distribution

$$(2.4) \qquad q(\mathbf{x}, \hat{\mathbf{v}}) := \frac{m(\mathbf{x}, \hat{\mathbf{v}})}{M(\mathbf{x})}$$

is, for each $\mathbf{x} \in \Omega$, the probability density function describing the statistical distribution of the directions of the fibers at $\mathbf{x} \in \Omega$. In particular, as the fibers are not polarized, we assume that q (and therefore m) is even as a function of $\hat{\mathbf{v}}$ for all $\mathbf{x} \in \Omega$, which implies that the average direction of the fibers vanishes:

$$\mathbb{E}_q := \int_{\mathbb{S}^{d-1}} q(\mathbf{x}, \hat{\mathbf{v}}) \hat{\mathbf{v}} \, d\hat{\mathbf{v}} = \mathbf{0}.$$

Moreover, we can introduce the variance-covariance matrix of q:

$$\mathbb{D}_q := \int_{\mathbb{S}^{d-1}} q(\mathbf{x}, \hat{\mathbf{v}}) \hat{\mathbf{v}} \otimes \hat{\mathbf{v}} \, d\hat{\mathbf{v}}.$$

The tensor $\mathbb{D}_q$ is symmetric and positive semidefinite. If it is positive definite, then it is diagonalizable. Equal eigenvalues correspond to an isotropic distribution of the ECM fibers. Conversely, an anisotropic distribution is characterized by different eigenvalues, with the leading eigenvector representing the direction of preferential orientation of ECM fibers. This allows one to reproduce isotropic/anisotropic migration on a nonpolarized fiber network [19, 32]. In particular, if q is the von Mises distribution, the corresponding variance-covariance matrix is positive definite.

2.1. Microscopic model. The individual dynamics of a cell may be described at the microscopic level by means of evolution equations for random variables taking into account the position $\mathbf{X}_t \in \Omega$, the speed $V_t \in [0, U]$, and the direction $\hat{\mathbf{V}}_t \in \mathbb{S}^{d-1}$ of a cell whose joint distribution function is $p(t, \mathbf{X}_t = \mathbf{x}, V_t = v, \hat{\mathbf{V}}_t = \hat{\mathbf{v}})$ for each t and $\mathbf{x}$. As classically done in kinetic theory, the microscopic dynamics of cell speed and direction are described by the means of *binary interactions.* In the present case, the ECM fibers are described by the random variables $\mathbf{Y}_t \in \Omega$ and $\hat{\mathbf{V}}_t^m \in \mathbb{S}^{d-1}$, whose distribution function is $m(\mathbf{Y}_t = \mathbf{y}, \hat{\mathbf{V}}_t^m = \hat{\mathbf{v}}^m)$.

In particular, the re-orientation mechanism related to the change of cell speed and direction may be described in terms of discrete in time stochastic processes [33] for the random variables V_t and $\hat{\mathbf{V}}_t$, which, during a time interval Δt, may change or not according to whether a re-orientation happens or not. These dynamics may be implemented in a discrete in time random process as

$$(2.5) \qquad \begin{cases} \hat{\mathbf{V}}_{t+\Delta t} = (1 - \Sigma)\hat{\mathbf{V}}_t + \Sigma \hat{\mathbf{V}}_t', \\ V_{t+\Delta t} = (1 - \Sigma)V_t + \Sigma V_t', \end{cases}$$

where Σ is a Bernoulli random variable with parameter $\mu B(\mathbf{Y}_t - \mathbf{X}_t)\Delta t$, saying whether a re-orientation, during which a cell changes both its direction and speed of motion, happens ($\Sigma = 1$) or not ($\Sigma = 0$). The quantity μ is the frequency of interaction with the ECM through the protrusions, while B is the interaction kernel that governs the rate at which an agent in position $\mathbf{X}_t$ (in this case the cell) interacts with an agent in position $\mathbf{Y}_t$ (a fiber of the ECM) and changes its velocity. This typically allows one to take into account non-local interactions in the physical space, meaning interactions between two agents located at a certain distance [13, 21]. In the present context, this is related to the cell's capability of sensing its neighborhood by interacting with/measuring the ECM population $m(\mathbf{y}, \hat{\mathbf{v}}^m)$, whose value will affect the new velocity after the re-orientation. We remark that in order for Σ to be well defined, we need $\Delta t \leq 1/(\mu B(\mathbf{Y}_t - \mathbf{X}_t))$, which means that for a high frequency μ there is a high probability of having a re-orientation during a given time interval Δt. As in [7], we assume that B has a compact support and that $\Delta t \leq \frac{1}{\mu \max B}$. The random variables V'_t and $\hat{\mathbf{V}}'_t$ denote the new speed and direction after a re-orientation. We also remark that we are assuming that there is a unique microscopic process driving re-orientation and that both direction and speed change simultaneously, and not independently, at each re-orientation. This assumption is related to the fact that we are considering a unique external factor (ECM) affecting speed and direction at the same time. Of course, other assumptions can be done, e.g., one can assume independent processes for the changes in direction and speed.

Classically, in kinetic theory, the microscopic dynamics are described through *interaction rules.* In general, such microscopic rules are written in the form

$$(2.6) \qquad V'_t = I(V_t, \hat{\mathbf{V}}_t, \hat{\mathbf{V}}^m_t) + \sqrt{D}\Theta, \qquad \hat{\mathbf{V}}'_t = \hat{I}(V_t, \hat{\mathbf{V}}_t, \hat{\mathbf{V}}^m_t) + \sqrt{\hat{\mathbb{D}}}\Xi,$$

where $I, \hat{I}$ describe the deterministic part, which may depend on both the pre-reorientation speed V_t and direction $\hat{\mathbf{V}}_t$, as well as on the orientation of the fiber $\hat{\mathbf{V}}^m_t$. D and $\hat{\mathbb{D}}$ are diffusion matrices, being $\sqrt{\hat{\mathbb{D}}}^T \sqrt{\hat{\mathbb{D}}} = \hat{\mathbb{D}}$, while Θ and Ξ are white noises, i.e., $\langle \Theta \rangle = \langle \Xi \rangle = 0$, $\langle \Theta^2 \rangle = \langle \Xi^2 \rangle = 1$. Here and hereafter, $\langle \cdot \rangle$ denotes the average operator with respect to all random variables appearing in brackets. As we assume no ECM re-modeling, we have that in a binary interaction the direction of the fiber does not change, i.e., $\hat{\mathbf{V}}^m_{t+\Delta t} = \hat{\mathbf{V}}^m_t$. This approach, also known as the *collisional* approach, which is classical in kinetic theory and in the literature of multi-agent systems, allows for detailed descriptions of the microscopic dynamics.

Remark. ECM fibers are assumed to remain constant, i.e., their state does not change after interacting with the cells. In this sense, this microscopic process may also be considered as an interaction with a *fixed background,* i.e., m is fixed. However, we have presented the microscopic process as a binary interaction process and an envisaged possible extension is to consider the evolution of the ECM fibers, which may describe the remodeling of the ECM.

Remark. Usually, in works where experimental and computer-based models are coupled (see, e.g., [17, 34]), the evolution of the cell velocity is described by considering the superposing effect of external forces $\mathbf{F}^{ext}$, modeled to take into account the influence of the external environment. In particular, these locomotive forces are determined by estimation from the data. This approach allows the use of open-source softwares such as Physicell [16], which is a hybrid 3D cell simulator that combines the model of the cellular environment (the chemical cues, the ECM mechanical behavior, etc.) as a continuum with an agent-based model for the cells. The approach we propose here allows us to start from an agent-based model in which

details about the microscopic dynamics may be implemented and then included in the macroscopic models that can be derived. In the modeling framework given by (2.6), I and $\hat{I}$ may be linked to the external forces acting on the cells by simply setting $V_{t+\Delta t}\hat{\mathbf{V}}_{t+\Delta t} = V_t\hat{\mathbf{V}}_t + \mathbf{F}^{ext}\Delta t$.

On the other hand, if we want to describe the microscopic process as a velocity-jump process, we need to consider transition probabilities as probability density functions of the random variables V_t' and $\hat{\mathbf{V}}_t'$ that are given by

$$(2.7) \qquad V_t' \sim \psi(V_t'|M(\mathbf{Y}_t)), \qquad \hat{\mathbf{V}}_t' = \hat{\mathbf{V}}_t^m \sim m(\mathbf{Y}_t, \hat{\mathbf{V}}_t^m).$$

Here, $\psi = \psi(v|M)$ is a probability density function of the speeds, conditioned by the ECM density M. It has an average speed $\bar{v}(M)$ depending on M and a second moment D_M such that its variance is $D_M - \bar{v}(M)^2$.

We then consider the kinematic relation for the variation of the position $\mathbf{X}_t$ during a time interval Δt given by

$$(2.8) \qquad \mathbf{X}_{t+\Delta t} = \mathbf{X}_t + \Delta t\mathbf{V}_t.$$

As already mentioned, the ECM is explored by the cell through its protrusions, which may be extended up to a maximum *sensing radius R*. As previously done in [26], in order to include physical limits of migration, we shall consider a non-constant sensing radius, identifying the fact that a cell cannot measure the external cue in a physical region that cannot be reached. In particular, the ECM density M_{th} represents this physical limit and we shall consider the non-constant sensing radius defined by [26]

$$(2.9) \qquad R_M(t,\mathbf{x},\hat{\mathbf{v}}) = \begin{cases} R & \text{if} \quad M(t,\mathbf{x}+\lambda\hat{\mathbf{v}}) \le M_{th} \quad \forall\lambda \in [0,R], \\ \inf\{\lambda \in [0,R] : M(t,\mathbf{x}+\lambda\hat{\mathbf{v}}) > M_{th}\} & \text{otherwise.} \end{cases}$$

The latter means that, in a given direction $\hat{\mathbf{v}}$, the sensing radius is limited as soon as the protrusion encounters a region through which the cell cannot migrate, while it is maximum if such a region, in a certain direction $\hat{\mathbf{v}}$, is not reached within a distance R. In particular, the sensing radius will affect the support of the interaction kernel, also called the Povzner kernel [13], namely

$$(2.10) \qquad B(\mathbf{y} - \mathbf{x}) = \delta(\mathbf{y} - (\mathbf{x} + \lambda\hat{\mathbf{v}}^m))\gamma(\lambda),$$

where $\gamma(\lambda)$ is a sensitivity function having compact support in $[0, R_M(t,\mathbf{x},\hat{\mathbf{v}}^m)]$. This models the fact that a cell in $\mathbf{x}$ measures the information given by m in each position $\mathbf{y} = \mathbf{x} + \lambda\hat{\mathbf{v}}^m$, i.e., along each direction $\hat{\mathbf{v}}^m$, with $\lambda \in [0, R_M(t,\mathbf{x},\hat{\mathbf{v}}^m)]$, and the information is weighted according to γ. In particular, γ may be a Dirac delta if the cell only evaluates the information on the tip of the protrusion, while it may be a characteristic function if the cell weights uniformly the information up to the tip of the protrusion. An illustration of the Povzner kernel is reported in Figure SM1. Hereafter, "SM" indicates supplementary materials (ConteLoy_SM_R1.pdf [local/web 1.92MB]), which are directly referenced from the main article webpage.

2.2. Mesoscopic model. Through a rather classical procedure [33], it is possible to derive a kinetic equation for the evolution of the distribution p describing the statistical distribution of cells obeying the microscopic process (2.5)–(2.8)–(2.10) joined with (2.6) or (2.7). Here, we report the main steps of the derivation, while a more detailed description of the procedure is provided in section SM1.

Let $\phi = \phi(\mathbf{x}, v, \hat{\mathbf{v}})$ be an observable quantity defined on $\Omega \times \mathcal{V}$, where we have introduced the notation $\mathcal{V} = [0, U] \times \mathbb{S}^{d-1}$ for brevity. We consider ϕ to be a $\mathcal{C}^\infty$ function having compact support, and we let Σ be the Bernoulli random variable with parameter $\mu B(\mathbf{Y}_t - \mathbf{X}_t) \Delta t$. From (2.5) together with the assumed independence of Σ, we see that the mean variation rate of ϕ in the time interval Δt satisfies

$$\frac{\left\langle \phi\left(\mathbf{X}_{t+\Delta t}, V_{t+\Delta t}, \hat{\mathbf{V}}_{t+\Delta t}\right) \right\rangle - \left\langle \phi\left(\mathbf{X}_t, V_t, \hat{\mathbf{V}}_t\right) \right\rangle}{\Delta t}$$
$$= \frac{\left\langle \phi\left(\mathbf{X}_t + V_t \hat{\mathbf{V}}_t \Delta t, V_t, \hat{\mathbf{V}}_t\right)(1 - \mu B \Delta t) + \phi\left(\mathbf{X}_t + V_t \hat{\mathbf{V}}_t \Delta t, V_t', \hat{\mathbf{V}}_t'\right) \mu B \Delta t - \phi\left(\mathbf{X}_t, V_t, \hat{\mathbf{V}}_t\right) \right\rangle}{\Delta t}.$$

Whence, we deduce the instantaneous time variation of the average of ϕ in the limit $\Delta t \to 0^+$ as

$$(2.11) \quad \frac{d}{dt} \left\langle \phi\left(\mathbf{X}_t, V_t, \hat{\mathbf{V}}_t\right) \right\rangle = \left\langle \mu B(\mathbf{Y}_t - \mathbf{X}_t) \left[\phi\left(\mathbf{X}_t, V_t', \hat{\mathbf{V}}_t'\right) - \phi\left(\mathbf{X}_t, V_t, \hat{\mathbf{V}}_t\right) \right] \right\rangle$$
$$+ \left\langle \nabla_{\mathbf{x}} \cdot \left(V_t \hat{\mathbf{V}}_t \phi(\mathbf{X}_t, V_t, \hat{\mathbf{V}}_t) \right) \right\rangle.$$

Here, on the right-hand side, the first two terms take into account the gain and loss terms related to the re-orientation process, respectively, while the last term accounts for the free particle drift. If the microscopic process ruling the evolution of V_t', $\hat{\mathbf{V}}_t'$ is the velocity jump process (2.7), then the gain term describing the new cell's speed and direction $(V_t', \hat{\mathbf{V}}_t')$ can be written as

$$\left\langle B(\mathbf{Y}_t - \mathbf{X}_t) \phi\left(\mathbf{X}_t, V_t', \hat{\mathbf{V}}_t'\right) \right\rangle$$
$$= \int_{\mathbb{R}} \int_{\Omega} \int_{\mathcal{V}} \left(\int_{\mathcal{V}} \gamma(\lambda) \phi(\mathbf{x}, v', \hat{\mathbf{v}}') \psi(v' | M(\mathbf{x} + \lambda \hat{\mathbf{v}}')) m(\mathbf{x} + \lambda \hat{\mathbf{v}}', \hat{\mathbf{v}}') \, d\hat{\mathbf{v}}' dv' \right)$$
$$(2.12) \qquad \times p(t, \mathbf{x}, v, \hat{\mathbf{v}}) \, d\hat{\mathbf{v}} \, dv \, d\mathbf{x} \, d\lambda,$$

while

$$\left\langle B(\mathbf{Y}_t - \mathbf{X}_t) \phi\left(\mathbf{X}_t, V_t, \hat{\mathbf{V}}_t\right) \right\rangle$$
$$(2.13) \qquad = \int_{\Omega} \int_{\mathbb{R}} \int_{\mathcal{V}} \phi(\mathbf{x}, v, \hat{\mathbf{v}}) \, p(t, \mathbf{x}, v, \hat{\mathbf{v}}) m(\mathbf{x} + \lambda \hat{\mathbf{v}}, \hat{\mathbf{v}}) \gamma(\lambda) \, d\hat{\mathbf{v}} dv d\lambda d\mathbf{x}$$

and

$$(2.14) \quad \left\langle \nabla_{\mathbf{x}} \cdot \left(V_t \hat{\mathbf{V}}_t \phi(\mathbf{X}_t, V_t, \hat{\mathbf{V}}_t) \right) \right\rangle = - \int_{\Omega} \int_{\mathcal{V}} \phi(\mathbf{x}, v, \hat{\mathbf{v}}) \, v\hat{\mathbf{v}} \cdot \nabla_{\mathbf{x}} p(t, \mathbf{x}, v, \hat{\mathbf{v}}) \, d\hat{\mathbf{v}} dv d\mathbf{x}.$$

Rewriting (2.11) with (2.12)–(2.13)–(2.14) and choosing $\phi(\mathbf{x}, v, \hat{\mathbf{v}}) = \xi(\mathbf{x}) \varphi(v, \hat{\mathbf{v}})$ in the kinetic equation for p, we obtain

$$\frac{d}{dt} \int_{\mathcal{V}} \varphi(v, \hat{\mathbf{v}}) p(t, \mathbf{x}, v, \hat{\mathbf{v}}) d\hat{\mathbf{v}} dv + \nabla_{\mathbf{x}} \cdot \int_{\mathcal{V}} \varphi(v, \hat{\mathbf{v}}) \mathbf{v} p(t, \mathbf{x}, v, \hat{\mathbf{v}}) \, d\hat{\mathbf{v}} dv$$
$$(2.15) \qquad = \eta \int_{\mathcal{V}} \left[\int_{\mathcal{V}} T[m](v', \hat{\mathbf{v}}') \varphi(v', \hat{\mathbf{v}}') \, d\hat{\mathbf{v}}' dv' - \varphi(v, \hat{\mathbf{v}}) \right] p(t, \mathbf{x}, v, \hat{\mathbf{v}}) d\hat{\mathbf{v}} dv,$$

where

$$(2.16) \qquad T[m](\mathbf{x}, v, \hat{\mathbf{v}}) = \int_0^{R_M(\mathbf{x}, \hat{\mathbf{v}})} \frac{m(\mathbf{x} + \lambda \hat{\mathbf{v}}, \hat{\mathbf{v}})}{\bar{M}(\mathbf{x})} \psi(v | M(\mathbf{x} + \lambda \hat{\mathbf{v}})) \gamma(\lambda) \, d\lambda$$

is a *transition probability* satisfying

$$\int_{\mathcal{V}} T[m](\mathbf{x}, v, \hat{\mathbf{v}}) \, d\hat{\mathbf{v}} \, dv = 1$$

and describing the probability for a cell located at $\mathbf{x}$ of choosing a speed v and direction $\hat{\mathbf{v}}$. This transition probability encodes the fact that a cell extends its protrusions and senses the ECM in each direction, collecting at the same time information regarding the fiber structure and macroscopic ECM density, and weights them in the same way. The strong form of (2.15) is

$$(2.17) \qquad \frac{\partial p}{\partial t}(t, \mathbf{x}, v, \hat{\mathbf{v}}) + \mathbf{v} \cdot \nabla_{\mathbf{x}} p(t, \mathbf{x}, v, \hat{\mathbf{v}}) = \mathcal{J}[p](t, \mathbf{x}, v, \hat{\mathbf{v}}),$$

which describes the evolution of the statistical distribution of the cells that obey the microscopic dynamics (2.7), where the right-hand side is the *turning operator*

$$(2.18) \qquad \mathcal{J}[p](t, \mathbf{x}, v, \hat{\mathbf{v}}) = \eta(\rho(t, \mathbf{x}) T[m](\mathbf{x}, v, \hat{\mathbf{v}}) - p(t, \mathbf{x}, v, \hat{\mathbf{v}})).$$

In (2.18), $\eta = \mu \bar{M}$ is the *frequency of re-orientation* at the population level, which depends not only on the frequency μ but also on the measured quantity of the ECM. The quantity

$$\bar{M}(\mathbf{x}) = \int_{\mathbb{S}^{d-1}} \int_0^{R_M(\mathbf{x}, \hat{\mathbf{v}})} m(\mathbf{x} + \lambda \hat{\mathbf{v}}, \hat{\mathbf{v}}) \gamma(\lambda) d\lambda d\hat{\mathbf{v}}$$

is, in fact, an average of the ECM density over the measured neighborhood, where the information is weighted by γ. We stress the fact that this particular transition probability (2.16) is the one implementing the microscopic process (2.5)–(2.7), in which cells change simultaneously both direction and speed, as they sense the same external cue m, influencing the choice of direction and speed through two different mechanisms. This is different from considering two independent sensings as in [25, 26], where the two measured quantities affecting the direction and the speed have different origins. The average velocity of the transition probability (2.16) is given by

$$\mathbf{U}_T(\mathbf{x}) = \int_{\mathcal{V}} T[m](\mathbf{x}, v, \hat{\mathbf{v}}) \, v \hat{\mathbf{v}} \, dv d\hat{\mathbf{v}}$$
$$= \int_{\mathbb{S}^{d-1}} \int_0^{R_M(\mathbf{x}, \hat{\mathbf{v}})} \frac{m(\mathbf{x} + \lambda \hat{\mathbf{v}}, \hat{\mathbf{v}})}{\bar{M}(\mathbf{x})} \bar{v}(\mathbf{x} | M(\mathbf{x} + \lambda \hat{\mathbf{v}})) \gamma(\lambda) \, d\lambda \, \hat{\mathbf{v}} \, d\hat{\mathbf{v}},$$

where $\bar{v}(\mathbf{x} | M(\mathbf{x} + \lambda \hat{\mathbf{v}}))$ represents the mean of the probability density function of the speed ψ, conditioned by the ECM density M, while the variance-covariance matrix is

(2.19)

$$\mathbb{D}_T(\mathbf{x}) = \int_{\mathcal{V}} T[m](\mathbf{x}, v, \hat{\mathbf{v}}) (\mathbf{v} - \mathbf{U}_T) \otimes (\mathbf{v} - \mathbf{U}_T) \, dv \, d\hat{\mathbf{v}}$$
$$= D_M \int_{\mathbb{S}^{d-1}} \int_0^{R_M(\mathbf{x}, \hat{\mathbf{v}})} \frac{m(\mathbf{x} + \lambda \hat{\mathbf{v}}, \hat{\mathbf{v}})}{\bar{M}(\mathbf{x})} \gamma(\lambda) \, d\lambda \, \hat{\mathbf{v}} \otimes \hat{\mathbf{v}} \, d\hat{\mathbf{v}} - \mathbf{U}_T(\mathbf{x}) \otimes \mathbf{U}_T(\mathbf{x}),$$

where D_M is the second moment of the probability density function ψ of the speeds. We assume that it is constant, as it is reasonable to assume that all the cells are affected with the same degree of stochastic variation.

Remark. If we want to implement the dynamics (2.6), then the gain term is

$$\left\langle B(\mathbf{Y}_t - \mathbf{X}_t)\phi\left(\mathbf{X}_t, V'_t, \hat{\mathbf{V}}'_t\right)\right\rangle$$
$$= \int_\Omega \int_\mathbb{R} \int_\mathcal{V} \int_{\mathbb{S}^{d-1}} \phi(\mathbf{x}, v', \hat{\mathbf{v}}') \, d\hat{\mathbf{v}}' dv' \gamma(\lambda) p(t, \mathbf{x}, v, \hat{\mathbf{v}}) m(\mathbf{x} + \lambda\hat{\mathbf{v}}^m, \hat{\mathbf{v}}^m) \, d\hat{\mathbf{v}}^m d\hat{\mathbf{v}} dv d\lambda d\mathbf{x},$$

with $v', \hat{\mathbf{v}}'$ given by (2.6), so that the kinetic equation is the Boltzmann–Povzner equation [35, 13]

$$\frac{d}{dt}\int_\mathcal{V} \varphi(v, \hat{\mathbf{v}})p(t, \mathbf{x}, v, \hat{\mathbf{v}})dvd\hat{\mathbf{v}} + \nabla_\mathbf{x} \cdot \int_\mathcal{V} \varphi(v, \hat{\mathbf{v}})\mathbf{v}p(t, \mathbf{x}, v, \hat{\mathbf{v}}) \, dvd\hat{\mathbf{v}}$$

$$(2.20) \qquad = \eta\left\langle\int_\mathcal{V} (\varphi(v', \hat{\mathbf{v}}') - \varphi(v, \hat{\mathbf{v}}))p(t, \mathbf{x}, v, \hat{\mathbf{v}}) \, dvd\hat{\mathbf{v}}\right\rangle.$$

In the case $B = 1$, choosing

$$(2.21) \qquad I(v, \hat{\mathbf{v}}, \hat{\mathbf{v}}^m) = \bar{v}(M), \ D = D_M - \bar{v}(M)^2, \quad \hat{I}(v, \hat{\mathbf{v}}, \hat{\mathbf{v}}^m) = \mathbb{E}_q, \ \hat{\mathbb{D}} = \mathbb{D}_q^T\mathbb{D}_q$$

in (2.6), then the evolution of the average and second moment of p prescribed by the model (2.20)–(2.6) is the same as if its evolution was ruled by (2.17)–(2.18)–(2.16). It is worth mentioning that the average and second moment of p are the ones that are involved in the hydrodynamic description of the system. Moreover, the microscopic model (2.5)–(2.6)–(2.8)–(2.10) with the choice (2.21) instead of (2.7) may be particularly useful in the case in which q and ψ are not easy to sample.

2.3. Macroscopic behavior. In order to investigate the overall trend of the system, the behavior of the statistical moments is typically analyzed. This is typically done through the derivation of evolution equations for at least $\rho(t, \mathbf{x})$ in the emerging regime of the system, which may result from a proper nondimensionalization. Formally, we introduce a small parameter $\epsilon \ll 1$ and we assume that up to a nondimensionalization the spatial variable $\mathbf{x}$ can be re-scaled as

$$(2.22) \qquad \boldsymbol{\xi} = \epsilon\mathbf{x},$$

$\boldsymbol{\xi}$ being the nondimensional spatial variable. According to the other characteristic quantities of the system and up to an appropriate nondimensionalization, the long time scale τ will be

$$(2.23) \qquad \tau = \epsilon^{3-\alpha}t.$$

The appropriate scaling of the system can be done by analyzing its dominant behavior, which can be investigated by measuring the mean squared displacement (MSD)

$$(2.24) \qquad MSD(t) := \langle||\mathbf{x}||^2\rangle$$

and determining its growth with respect to time, i.e.,

$$(2.25) \qquad \langle||\mathbf{x}||^2\rangle \sim t^\alpha,$$

where the following hold:
- $\alpha = 1$ indicates a diffusion dominated phenomenon (purely diffusive);
- $\alpha = 2$ indicates a drift dominated phenomenon (purely directed).

The two choices correspond to a parabolic scaling ($\tau = \epsilon^2 t$) and to a hyperbolic scaling ($\tau = \epsilon t$), respectively.

Remark. In the present case, we want to derive the evolution equation for the statistical moments at the same spatial scale of the experiments, i.e., at the microscopic spatial scale. Hence, the formal diffusive/hyperbolic scaling is meant as the result of a nondimensionalization classically leading to

$$\text{St}\partial_t p + \mathbf{v} \cdot \nabla_{\mathbf{x}} p = \frac{1}{\text{Kn}} \mathcal{J}[p],$$

where St is the Strouhal number defined as $\text{St} = \frac{\tilde{l}}{\tilde{v}\tilde{t}}$, where $\tilde{l}, \tilde{v}, \tilde{t}$ are reference length, velocity, and long time scale, respectively, while $\text{Kn} = \frac{\tilde{v}}{\tilde{l}\eta}$ is the Knudsen number. Let us consider $\tilde{l} = \mathcal{O}(1)$ so that we are actually looking at the microscopic spatial scale and the sensing radius does not need to be rescaled, and let us suppose that the Knudsen number is small, i.e., $\text{Kn} = \epsilon$. Therefore, if $\text{St} = \epsilon$, this corresponds to $\tilde{t} = \frac{\epsilon^{-2}}{\mu}$ (diffusive), while if $\text{St} = 1$, this corresponds to $\tilde{t} = \frac{\epsilon^{-1}}{\mu}$ (hyperbolic).

There are a number of limit techniques relying on Hilbert expansions for transport equations with velocity jump processes that have been widely treated in [19, 20, 25, 26, 30]. They are based on expansions of the transition probability up to the re-scaling (2.22) as

$$T(\boldsymbol{\xi}, v, \hat{\mathbf{v}}) = T_0(\boldsymbol{\xi}, v, \hat{\mathbf{v}}) + \epsilon T_1(\boldsymbol{\xi}, v, \hat{\mathbf{v}}) + \mathcal{O}(\epsilon^2)$$

and, consequently, of its average $\mathbf{U}_T^i$ in (SM2.2), of the variance-covariance matrix $\mathbb{D}_T^i$ in (SM2.3), and of the distribution function p in (SM2.4). In particular, the fundamental property for performing the diffusive limit requires that the leading order of the drift vanishes, i.e.,

(2.26) $$\mathbf{U}_T^0 = 0.$$

Carrying out the asymptotic procedure leads to

(2.27) $$\frac{\partial}{\partial \tau}\rho + \nabla \cdot (\mathbf{U}_T^1 \rho) = \nabla \cdot \left[\frac{1}{\eta}\nabla \cdot (\mathbb{D}_T^0 \rho) \right],$$

$\mathbb{D}_T^0$ being the diffusion motility tensor given by leading order of the variance-covariance matrix in (SM2.3). Equation (2.27) is a diffusion-advection equation, where $\mathbf{U}_T^1$ is the drift velocity of first order.

If (2.26) does not hold, as typically happens if the sensing radius R is large with respect to the length of variation of the external field m, but the nondimensionalization of the system or experimental observations prescribe a diffusive regime, we can consider a drift-diffusion limit, as was done in [24]. Setting $p(\tau, \boldsymbol{\xi}, \mathbf{v}) = u(\tau, z, \mathbf{v})$, with $z = \boldsymbol{\xi} - \mathbf{U}_T\tau$, we have

$$\frac{\partial}{\partial \tau}p + \mathbf{v} \cdot \nabla p = \mathcal{L}[p] \iff \frac{\partial}{\partial \tau}u + \nabla \cdot ((\mathbf{v} - \mathbf{U}_T)u) = \mathcal{L}[u]$$

(2.28) $$\frac{\partial}{\partial \tau}\rho + \nabla \cdot (\mathbf{U}_T \rho) = \nabla \cdot \left(\frac{1}{\eta}\nabla \cdot (\mathbb{D}_T \rho) \right).$$

If, instead, a hyperbolic scaling is required, we can use the results presented in [19], which gives

(2.29) $$\frac{\partial}{\partial \tau}\rho + \nabla \cdot (\rho \mathbf{U}_T) = \varepsilon \nabla \cdot \left(\frac{1}{\eta}\nabla \cdot (\mathbb{D}_T \rho) + \frac{1}{\eta}\rho \mathbf{U}_T \nabla \cdot \mathbf{U}_T \right).$$

This is the equation with the first-order correction in which we can recover the dependency on the ECM through the frequency η in the correction term.

For the reader's convenience, more details about the well-known techniques required for the asymptotic procedures are reported in section SM2.

3. Numerical investigations. In this section, we present some numerical tests. In particular, we shall integrate numerically

- the microscopic model (2.5)–(2.8)–(2.10) with (2.6)–(2.21) or, equivalently, with (2.7), with Monte Carlo methods as in [28];
- the kinetic model (2.17)–(2.18)–(2.16) with the same method used in [9, 25, 26];
- the macroscopic diffusion and drift-diffusion models (2.27) or (2.28) with a continuous Galerkin finite element scheme [41], while the drift model (2.29) with a Donor-cell advection scheme [23].

We shall consider no flux boundary conditions. In particular, four numerical tests are presented.

Test 1 In section 3.1, we validate the microscopic model (2.5)–(2.8)–(2.10) with the choice (2.7) (with $B = 1$, as we are on a spatially homogeneous setting) by comparing our simulations with the experimental results presented in [34], where the authors investigate the phenomenon of steric hindrance on collagen gel. We remark that, as we are in a homogeneous setting, the microscopic model (2.5)–(2.8) with the choice (2.6) forecasts the same mass and average velocity for a large number of particles and a small Δt.

Test 2 In section 3.2, we consider an application of our microscopic model to the invasion of breast cancer cells from an aggregate into the collagen according to the experiments presented in [50]. We compare the results of the microscopic and kinetic models, and we also provide comparisons with the corresponding macroscopic limits.

Test 3 In section 3.3, we apply our model to investigate and make predictions on the dynamics of cells moving on collagen fibers with different densities and fiber alignment.

Test 4 In section 3.4, we use the kinetic model to investigate heterogeneous environments with an interface dividing regions with different collagen densities and/or fiber alignment. This is a more qualitative analysis, which shows the potential applicability of the proposed approach.

Major details for each test are presented in section SM3.

3.1. Steric hindrance on collagen gel. First, we consider the experimental results presented in [34]. Here, the authors track every 20 minutes for 24 hrs 50 NSCLC (Non-Small Cell Lung Cancer) cells moving on a 3D collagen-based matrix, made up of a collagen type I from bovine skin media of different densities. In particular, time-lapse images are acquired from the focal plane located in the middle of the z-axis, while out-of-focus cells are not quantified. Thus, the performed analysis on cell motility is substantially quantified in a 2D scenario. These experiments show how collagen density affects the strength of the physical barrier. Precisely, it interferes with cell migration by trapping single metastatic NSCLC cells and preventing their dissemination through the matrix. The authors find that for increasing values of the ECM density, the cell mean speed decreases and, correspondingly, the MSD becomes lower. They consider fixed collagen concentrations of 2.5 mg/mL, 4 mg/mL, and 6 mg/mL and measure the corresponding mean speeds, given by $\bar{v}(M) = [0.1696, 0.104, 0.063]\, \mu m/min$. Looking at the cell tracking graphs reported in [34], we observe a clear difference in the cell spreading when the value of M increases, showing reduced motility for higher values of the matrix density and a greater

spreading along the horizontal direction. We use the presented modeling framework to perform *in silico* tests and replicate the *in vitro* experiments of [34], looking at the minimal combination of ingredients that would allow us to obtain comparable results.

To this aim, we analyze three different settings:

i) M-dependent frequency η for the cell turning, a uniform speed distribution, and a random fiber network;

ii) M-dependent frequency η and speed distribution $\psi(v|M)$, combined with a random fiber network;

iii) M-dependent frequency η, speed distribution $\psi(v|M)$, and aligned fiber network.

As we expect from theoretical results [31], in this simplified case, using the kinetic model implementing the prescribed microscopic dynamics, we can compute the explicit form of the mean square displacement (MSD) that is proportional to the quadratic speed and inversely proportional to the re-orientation frequency, which, in the present case, is proportional to the matrix density M. Therefore, we expect an increasing MSD when decreasing the matrix density or increasing the mean speed. Considering the same experimental settings proposed in [34], for each case, we investigate the MSD of the cells and report the cell tracking in case iii), obtained with the integration of (2.5)–(2.8)–(2.10) with (2.7) (see Figure 1). Moreover, we evaluate the variation of cell mean and effective speed in relation to the ECM density.

In our *in silico* experiments (Figure 1), we observe that only choosing a non-uniform speed distribution (cases ii) and iii)), where we impose the measured mean
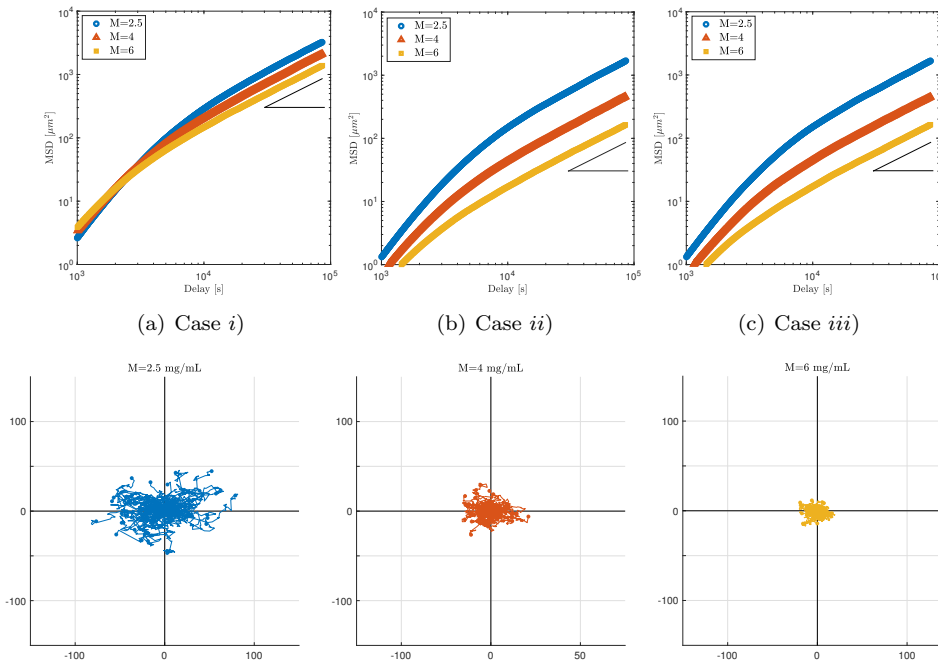

(a) Case *i*)   (b) Case *ii*)   (c) Case *iii*)

FIG. 1. **Test 1**. *Cell MSD (first row) in the cases* i), ii), iii) *and tracking (second row) in the domain* Ω *in the case* iii)*, with aligned fibers in the direction* $\theta_q = 0$*. For the MSD, the macroscopic densities* $M = [2.5, 4, 6]\,mg/mL$ *are considered in the following cases:* i) *uniform speed and random fibers in* (a)*;* ii) *M-dependent speed and random fibers in* (b)*;* iii) *M-dependent speed and aligned fibers in* (c)*. For cell tracking, we consider a Gaussian distribution for the speed. The parameter* k *describing the alignment strength is here set to* $k = 1.2$*. Simulations are run for* 24 *h with* $\Delta t = 0.0167\,h$*.*

speeds $\bar{v}(M)$, allows us to recover the appropriate reduced motility for higher values of the ECM density. Instead, the mere dependence of the frequency η on the ECM density M is not enough for recovering the MSD behavior observed experimentally (Figure 1, first line). A non-uniform speed distribution is also necessary to get the different behavior of the mean speed reported in the experiments (see Table SM1). Moreover, if the probability density function ψ is a truncated Gaussian distribution, we also recover the effective speeds (see Table SM2). We can observe a comparable directionality between the tracking when also an aligned fiber network is included. To reproduce cell alignment along a specific direction, a non-random description of the fiber network is necessary, i.e., case iii). Figure 1 shows the results of the cell tracking when fibers aligned along the direction indicated by $\theta_q = 0$ are included (tracking results related to the case ii) are shown in Figure SM3).

3.2. The influence of steric hindrance on human breast cancer cell migration. We now consider the experimental results obtained in [50], where the authors investigate how the physical properties of the ECM affect cancer cells' escape and invasion, using a microfluidic-based strategy (similar to the experiments in [34]) on human breast cancer cells within a type I collagen gel. This culture model was developed to observe the invasion of breast cancer cells from an aggregate into a collagen gel under interstitial flow, which mimics the initial stage of breast tumor progression. Precisely, they consider tumors that are formed adjacent to empty cavities (mimicking the blind end of a lymphatic vessel) and observe how tumor cell behavior changes in response to different ECM density values. By altering the stiffness, the pore size— and hence the density of the collagen gel—and the magnitude of the interstitial flow through the gel, they find that the pore size is the main physical factor that determines the rate at which cells escape from their initial aggregate and invade the cavity. In particular, the movement of 400 cancer cells through the collagen for two different collagen densities has been tracked over a period of 16 days, showing how a lower collagen concentration promotes a faster tumor escape towards the empty cavity.

We perform *in silico* tests in order to replicate the *in vitro* experiments performed in [50], where the authors measure the temporal evolution of the distance between the tumor and the cavity (details in section SM3.2). The *in silico* experiments are performed by running numerical simulations of the microscopic model (2.5)–(2.8)–(2.10) with the choice (2.7) (with $B = 1$, as we are on a spatially homogeneous setting) where ψ is given by (SM3.2) and q is the unimodal von Mises distribution with $\theta_q = 0$. This choice of q mimics the presence of an oriented interstitial flow. We set $k = 0.5$ in order to recover the experimental results reported in [50]. Results of the microscopic simulations are shown in Figure 2. In particular, the distance is defined as the distance between the cavity and the first, closer to the cavity, cell of the advancing cell aggregate. We report a graphical illustration of the setting used for the numerical simulations in Figure SM4.

We observe how the microscopic model, with a unique alignment parameter k, is able to reproduce the trend in both collagen densities. The experimental results and the 25th and 75th percentiles are reported not for a direct comparison but for showing that the difference in the rates of invasion in the two collagen densities is quite well reproduced.

In order to investigate more accurately the statistical evolution of the cells under the dynamics imposed by the microscopic model, we consider the kinetic model (2.17)–(2.18)–(2.16) and try to perform the same experiment. In this case, as we cannot track single cells, we need to impose a threshold for ρ in order to compute the distance of
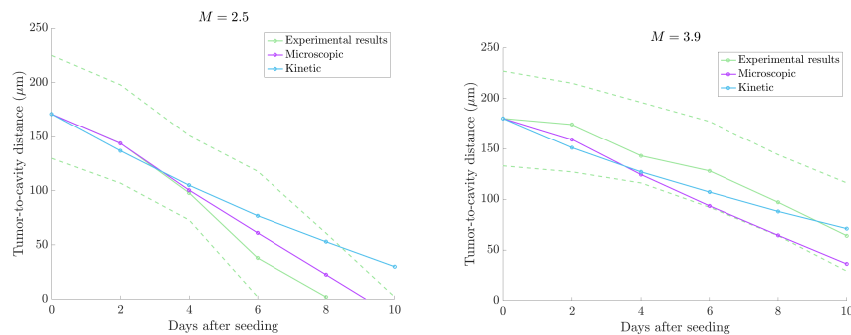
FIG. 2. **Test 2**. *Tumor-to-cavity distance as a function of time in low-density (left plot) and high-density (right plot) collagen. Light green solid lines represent the median values of the experimental setting, while light green dashed lines represent the 25th and 75th percentiles. Purple solid lines represent the median values of the microscopic numerical experiments, while blue solid lines represent the results of the kinetic model. We set $\mu = 0.0003\,1/min$, while the mean speeds are the ones measured in [50]: $\bar{v}(M) = 0.0166\,\mu m/min$ for $M= 2.5\,mg/mL$, while $\bar{v}(M) = 0.0137\,\mu m/min$ for $M= 3.9\,mg/mL$. Simulations are run for 10 days with $\Delta t = 7 \cdot 10^{-3}$ days.*

the advancing cell aggregate from the cavity. In particular, we choose $\rho_{th} = \frac{1}{400} = 2.5 \cdot 10^{-3}$, 400 being the number of cells used in the experiment. In particular, in Figure 2, we remark a good agreement with the microscopic model, even though we cannot observe a perfect superposition. This, of course, corresponds to what we know from the theory, as the kinetic model (2.17)–(2.18)–(2.16) is derived from the microscopic model (2.5)–(2.7)–(2.8)–(2.10) in the limit $N \to \infty$ and $\Delta t \to 0^+$, while here the simulation is run for 73×400 and 55×400 particles. This aspect also shows the convenience of using the kinetic model instead of the microscopic one. In fact, it allows us to obtain a complete statistical portrait with only one simulation, thus gaining a lower computational cost, instead of performing multiple simulations of the microscopic model or a simulation with a high N and very small Δt, which may be computationally challenging.

In Figure 3 (right plot), we plot a section of the cell density evolution along the x-axis. In particular, we plot the solution of the kinetic model (in blue), which we recover from the definition (2.1), and the solution of the microscopic model $\rho^{MC}(x,t)$, which we have run with $N = 10^6$ particles and $\Delta t = 0.001$ days. We construct the solution $\rho^{MC}(x,t)$ building the corresponding histograms both with 20 points (purple circles) and 1000 points (light green circles) over the interval $[0, 1000]\,\mu m$. We remark that there is an excellent agreement, as expected, between the solution $\rho^{MC}(x,t)$ of the microscopic model (2.5)–(2.7)–(2.8)–(2.10) and the solution $\rho(x,t)$ of the kinetic model (2.17)–(2.18)–(2.16). Always intending to reduce the computational effort, we look for the appropriate macroscopic model. To this aim, we observe the MSD shown in Figure 3 (left plot). For completeness, we look at both the microscopic and the kinetic models and we also report the lines $y = t$ (dashed green) and $y = t^2$ (dotted green) for direct comparison. We observe that the MSD prescribed by the microscopic (and, consequently, by the kinetic) model does not correspond to either a diffusive or a purely directed behavior. Diffusive or purely directed limits appear relevant on smaller time windows of cell evolution (early or late stages, respectively) without being able to reproduce the overall cell dynamics. Therefore, these limits cannot be used for predicting accurately the behavior of the macroscopic quantities. Instead, microscopic and kinetic models appear to be more accurate in predicting such behaviors, showing
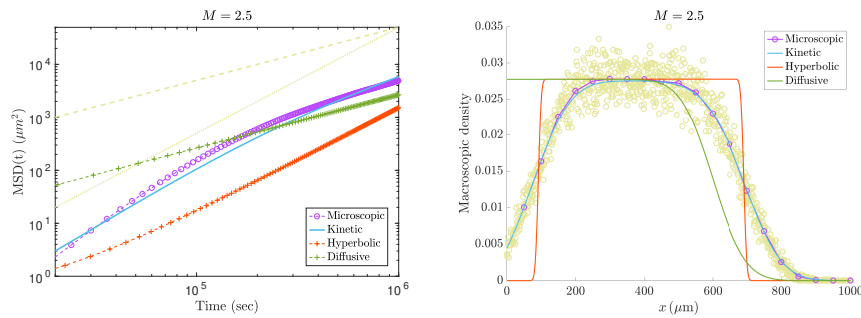
Fig. 3. ***Test 2***. *Mean squared displacement (MSD) and profile solutions for a fixed collagen density $M = 2.5\,mg/mL$. On the left, we compare the mean squared displacements prescribed by the microscopic (purple), kinetic (blue), hyperbolic (orange), and diffusive (green) limits, respectively. We also report the lines $y = t$ (light green dashed), $y = t^2$ (light green dotted). On the right, we plot a one-dimensional section of the solution along the x-axis for the microscopic, kinetic, hyperbolic, and diffusive models, with the same choice of colors done for the MSD. In particular, for the microscopic model we build the corresponding histograms over both 20 points in $[0, 1000]\mu m$ (purple circles) and 1000 points (light green circles) and we construct the solution from them.*

the relevant and the major levels of detail that these approaches are able to take into account. As a consequence, in Figure 3 (right plot), the solution of the hyperbolic model (2.29) (in orange) and the diffusive model (2.28) (in green) done with $\varepsilon = 10^{-3}$ do not reproduce accurately the solution of the kinetic model (2.17)–(2.18)–(2.16).

3.3. The interplay of steric hindrance and fiber alignment. We now use our model to investigate the interplay between steric hindrance and fiber alignment. Precisely, we analyze how cell migration on collagen fibers varies with respect to different combinations of matrix densities and fiber alignment. The main motivation for this test comes from a series of biological experiments that study separately the impact of stromal collagen concentration [40] and collagen alignment [38] on tumor local formation and invasion, where quantifications of the combined effects are underinvestigated. In particular, in [38], the authors use mouse breast tumor models to observe and define three tumor-associated collagen signatures (TACS), which are considered markers to locate and characterize tumor invasion. Specifically, TACS-1 refers to the presence of locally dense collagen randomly disposed fibers within the globally increased collagen concentration surrounding tumors; TACS-2 is defined as straightened collagen fibers stretched around the tumor and constraining its volume; TACS-3 identifies radially aligned collagen fibers that facilitate local invasion. These observations allow the use of collagen alignment to quantify local invasion. Furthermore, in [40], the authors extend the analysis, looking at the influence of the ECM on breast carcinoma development using a tumor model with increased stromal collagen in mouse mammary tissue. They demonstrate how this increased collagen, coupled with the different collagen-associated signatures, significantly increases tumor formation and results in a more invasive phenotype. Directed cell migration by contact guidance in aligned collagenous ECM has been also observed in [43], where the authors propose a method to align collagen gels, providing a controlled microenvironment for *in vitro* experiments. They quantify breast cancer cell behavior in these anisotropic constructs, showing how motility is enhanced in aligned collagen matrices and for a subpopulation of carcinoma cells, namely cancer stem cells (CSCs). In particular, these cells are characterized by smaller cell size and a high degree of phenotypic

plasticity, which makes them more able to adapt to contact-guided migration. We focus on the results in [43] concerning cell motility with respect to the alignment of the fibers and the density of the ECM. In particular, for our analysis we translate the differences in the cell size between cancer cells and CSCs as a difference in the matrix pore size, meaning that we expect to observe enhanced migration in less dense regions (where the pore size is bigger). We consider three different values of the ECM density, as given in [50], and the corresponding mean speeds. The values of the mean speeds are marked by the three blue stars in Figure SM6, where the black straight line represents the interpolating polynomial of degree two that may be considered to approximate the mean speed behavior as a function of the ECM density [4, 51]. We remark that, as in [50], we have an optimal matrix density corresponding to the maximum possible speed, while for smaller values of the ECM density the speed is lower because this corresponds to larger pores and to less efficient cell migration, as shown in [51]. The value of the mean speed also decreases for higher values of the ECM density because of the effect of the physical limit of migration [51]. We study the effects of matrix density and fiber alignment on cell mean speed $\bar{v}(M)$ and cell motility Υ in the direction of the alignment, defining cell motility as

$$\Upsilon(t) := \frac{MSD(t)}{t}.$$

Following [43], we compare the values of cell motility and mean speed after $\bar{T} = 16\,h$. We report a graphical illustration of the setting used for the numerical simulations in Figure SM5. Results of the simulations of the kinetic model (2.17)–(2.18)–(2.16) in this setting are shown in Figure 4.

In agreement with the results in [43], we observe how, for the same value of collagen density M, a stronger alignment of the fibers enhances the cell mean speed along the fiber tracks and this determines increased motility in the same direction, compared with the control case $k = 0$. In particular, the differences in both $\bar{v}(M)$ and Υ are more evident for $M = 2.5\,mg/mL$ and $3.2\,mg/mL$, while for $M = 3.9\,mg/mL$ the matrix density seems to be a greater obstacle for cell migration, even in strongly aligned environments. Comparing, instead, the cell behavior for the fixed value of the fiber alignment, we notice how the results about both mean speed and motility are in accordance with the relation $\bar{v}(M)$ illustrated in Figure SM6 and we obtain a greater mean speed and motility for $M = 3.2\,mg/mL$. In particular, comparing the left and right plots of Figure 4, we notice that the effect of the alignment on the mean speed seems to be lower than its effect on the cell motility, as was also observed in [43].
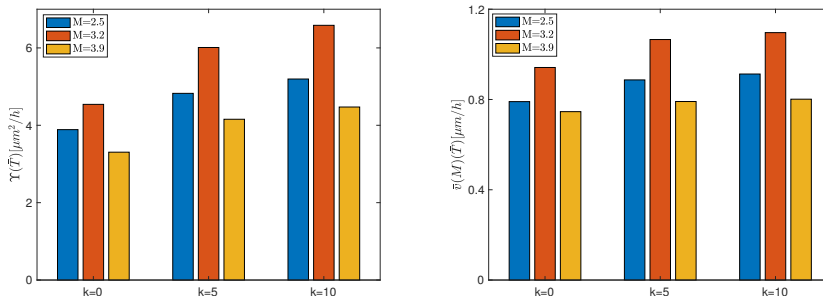

FIG. 4. **Test 3**. *Cell motility (Υ) and cell mean speed ($\bar{v}(M)$) in the direction $\theta_q = 0$ at $\bar{T} = 16\,h$ for three different values of the collagen density $M = 2.5, 3.2, 3.9\,mg/mL$ and three different values of the fiber alignment strength $k = 0, 5, 10$.*

Concerning the interplay between contact guidance and steric hindrance, this shows a prominent role of contact guidance in the overall dynamics.

3.4. The interplay of steric hindrance and fiber alignment in heterogeneous environments. In this test, we want to show the potential of the proposed model to study cell behavior in heterogeneous environments with both the effects of fiber alignment and steric hindrance on cell migration. We propose this test because non-locality is of the utmost importance in the presence of strongly heterogeneous environments. The heterogeneity can be related to both the fiber structure [18], as it may occur in the presence of different TACS or at the tumor-stroma interface [2, 38], and the presence of interfaces between different ECM density/porosity regions [45].

Experimentally, the main motivation for this test comes from [18], where the authors use a composite ECM made up of collagen of type I and matrigel to determine the influence of the local collagen fiber orientation on the collective intravasation ability of breast cancer cells. They build a controllable and heterogeneous landscape with a homogeneous distribution of fibers inside the collagen and fibers vertically orientated near the interface between the collagen and the matrigel regions. They show how cells follow the local fiber alignment direction during the intravasation into rigid matrigel and how an oriented fiber network could lead to a significantly enhanced infiltration potential. These results allow them to suggest the possibility of manipulating the ECM fiber structure orientation in the tumor microenvironment in order to alter and minimize the intravasation rate. The framework that we propose allows us to actually analyze not only the impact of a heterogeneous landscape of fibers, but also to combine it with the effects of different collagen densities.

As a first scenario, we consider a domain Ω divided into two subregions Ω_1 and Ω_2. In Ω_1, we consider an isotropic distribution of fibers, while in Ω_2 we assumed that the fibers are oriented in the direction $\theta_q = 0$. Moreover, we consider two different values of matrix density $M_1 = 2.5\,mg/mL$ and $M_2 = 9.9\,mg/mL$ and the corresponding values for the mean speeds $\bar{v}(M_1) = 0.1696\,\mu m/min$ and $\bar{v}(M_2) = 0.01\,\mu m/min$. The cells are initially placed at the interface between the two regions Ω_1, Ω_2. We analyze the behavior of the cells in two different cases. In the first one, we assume that in Ω_1 we have the matrix density M_1, while in Ω_2 we have the matrix density M_2. In the second one, instead, we invert the values of the matrix density, setting M_2 in Ω_1 and M_1 in Ω_2. The initial configuration of fibers and cells used in this setting is shown in Figure SM7. Concerning the sensing function γ in (2.16), we preliminarily choose for this test a Delta function. The qualitative evolution of the macroscopic cell density obtained by solving the kinetic model (2.17)–(2.18)–(2.16) in this setting is shown in Figure 5. The first row represents the case in which we set M_1 in Ω_1 and M_2 in Ω_2, while the second row represents the case M_2 in Ω_1 and M_1 in Ω_2. In both cases, we observe how in the region with collagen density M_2 (subregion Ω_2 for the first row setting while subregion Ω_1 for the second row setting) the migration of the cells is highly reduced, while it is promoted toward the region where the collagen density is set to M_1. Moreover, we can observe that the way cells invade this region differs between the two experiments due to the underlying distribution of the fibers. In fact, the isotropic fiber distribution in Ω_1 determines a more homogeneous spreading of the cells, while the anisotropic fiber distribution in Ω_2 determines a stronger cell alignment along the direction $\theta_q = 0$. Furthermore, we notice the effect of non-locality in the cell sensing of the microenvironment. In fact, in both cases, cells that are initially
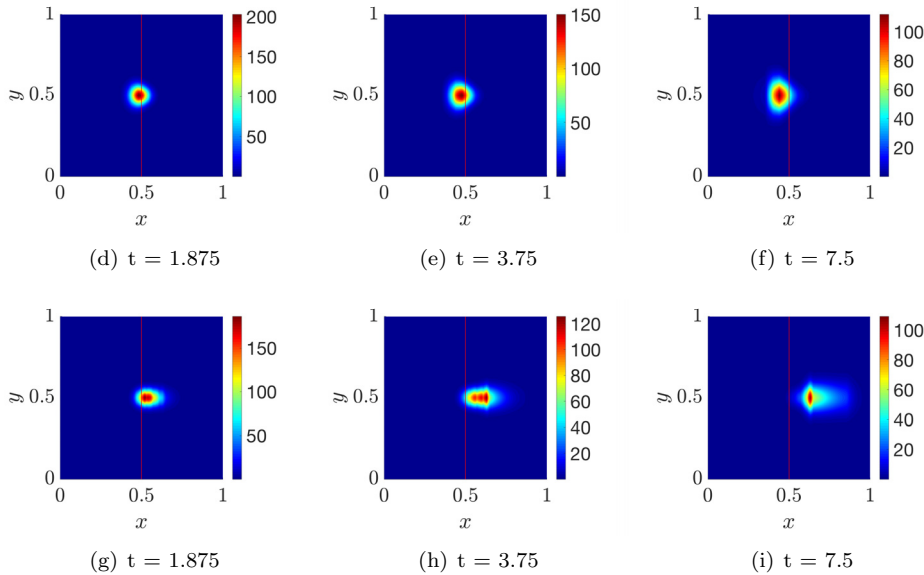
(d) t = 1.875   (e) t = 3.75   (f) t = 7.5

(g) t = 1.875   (h) t = 3.75   (i) t = 7.5

FIG. 5. **Test 4**. *Qualitative evolution of the macroscopic cell density obtained from* (2.17)–(2.18)–(2.16) *with an initial Gaussian distribution of cells with mean* $(x_0, y_0) = (0.5, 0.5)$ *and variance* $\sigma^2 = 10^{-3}$. *The sensing function is* $\gamma = \delta(R - \lambda)$. *The first row refers to the case* M_1 *in* Ω_1 *and* M_2 *in* Ω_2, *while the second row refers to the case* M_2 *in* Ω_1 *and* M_1 *in* Ω_2.

located in the region with the highest matrix density, but that are close enough (i.e., located at a distance lower than the sensing radius $R_M(t, \mathbf{x}, \hat{\mathbf{v}})$ from the interface) to sense the environment in the more favorable region, move towards it, instead of getting stuck due to the physical obstacle determined by the dense matrix. This is particularly clear if we compare these results with the evolution of the nonlocal kinetic model (2.17)–(2.18)–(2.16) with $\gamma = \delta(\lambda - 0)$, shown in Figure SM8, in which cells in the unfavorable region are not actually able to escape from it and their migration results are highly limited.

As a second scenario (Figure 6), we consider a different Ω divided into two subregions Ω_1 (above the red line) and Ω_2 (below the red line). Starting from the central point $(x_0, y_0) = (0.5, 0.5)$, we consider radially distributed fibers, while we consider two different values of matrix density: in Ω_1, $M_1 = 6\,mg/mL$, while in Ω_2, $M_2 = 10.35\,mg/mL$. The corresponding values for the mean speeds are $\bar{v}(M_1) = 0.0630\,\mu m/min$ and $\bar{v}(M_2) = 0.0002\,\mu m/min$. The cells are initially placed at the interface between the two regions Ω_1 and Ω_2, and the initial configuration of fibers and cells used in this setting is shown in Figure SM7. The qualitative evolution of the macroscopic cell density is shown in Figure 6. We observe how in the region with collagen density M_2 (i.e., Ω_2) the migration of the cells is almost nullified, while it is highly enhanced in the region where the collagen density is set to M_1 (i.e., Ω_1). Moreover, the way cells invade this region is driven by the underlying distribution of the fibers. In fact, their radial distribution is reflected in the radial spreading of the cells. Furthermore, as observed in the previous case, we notice the effect of nonlocality in cell sensing of the microenvironment. In fact, cells initially located in the region Ω_2, but that are close enough to sense the environment in Ω_1, move towards it, instead of getting stuck due to the dense matrix M_2.
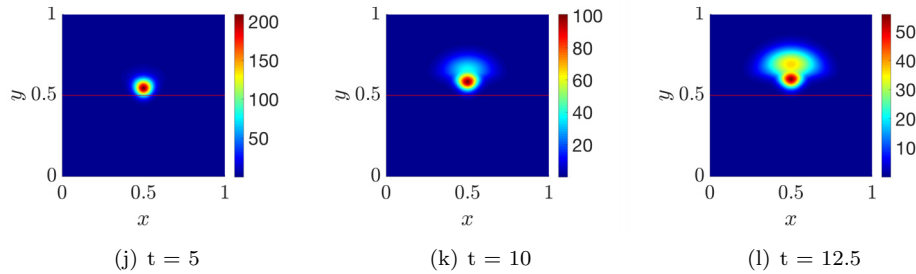
(j) t = 5   (k) t = 10   (l) t = 12.5

FIG. 6. **Test 4**. *Qualitative evolution of the macroscopic cell density obtained from* (2.17)–(2.18)–(2.16) *with an initial Gaussian distribution of cell with mean* $(x_0, y_0) = (0.5, 0.5)$ *and variance* $\sigma^2 = 10^{-3}$. *The sensing function is* $\gamma = \delta(R - \lambda)$.

4. Conclusion. In this work, we have presented a mathematical model for the description of contact guidance and steric hindrance, two fundamental mechanisms related to cell migration on the ECM. This model relies on a non-local (in the physical space) sensing of the ECM that allows us to take into account the role of cell protrusions, which may be extended up to several cell diameters, in heterogeneous environments. Considering the success of kinetic models for describing cell motion, especially because of their genuine multiscale nature, we have transferred existing mathematical methodologies of kinetic equations for multi-agent systems, already widely applied in other fields [7, 33], to the context of cell migration. Starting from microscopic discrete in time stochastic processes, which also involve non-local aspects, we have accurately described the microscopic dynamics and, then, formally derived a kinetic model implementing the chosen dynamics in the form of a collision-like Boltzmann equation. In particular, we have established the parallelism between this class of models and the velocity-jump processes, already commonly used to describe cell migration. This has allowed us not only to give a more detailed microscopic description of the considered dynamics, but also to obtain a microscopic algorithm for simulating them and, thus, performing *in silico* experiments.

The kinetic model that we have formally derived gives the complete statistical description of the system under study, and it implements exactly the prescribed microscopic dynamics, instead of postulating them at the mesoscopic scale. Moreover, this kinetic formulation allows us to run a unique simulation instead of performing multiple independent simulations.

We have shown how to derive from the mesoscopic level the macroscopic models in different regimes according to the system parameters ruling the different involved phenomena. In particular, this has allowed us to show how sometimes diffusive or advective models cannot be reliable to make accurate predictions and, thus, models directly stated at the macroscopic level could not be able to correctly describe cellular behaviors. We also remark that the established parallelism with the collisional Boltzmann equation can be used in order to inherit all the analytical tools that are widely used in the community of multi-agent systems and kinetic equations. In particular, it is also used to tackle technical difficulties that may be encountered in more complex models implementing velocity-jump processes, such as the determination of stationary equilibria and the derivation of macroscopic limits.

We have applied our model to the study of steric hindrance and contact guidance in several 3D scenarios related to breast cancer dissemination, which is a prominent medical issue. In fact, many efforts have been done, especially in the medical and

biological community, for the study of this process, but most of the difficulties are still encountered in the design of effective experimental platforms. Thus, our approach aims at providing a useful platform for performing *in silico* experiments. To this aim, and especially for what concerns steric hindrance, we have first validated our microscopic model studying the minimal and essential mechanisms that should be included at the microscopic level in order to retrieve several experimental results [34, 50]. Then, we have performed further experiments that couple the two mechanisms, namely steric hindrance and contact guidance. This has allowed us to make some predictions on the behavior of cells that undergo both mechanisms. In particular, the obtained results can actually be supported by biological evidence.

For completeness, we have to highlight that we have focused our attention on breast cancer dissemination, but the two considered mechanisms are involved in many other processes. The fundamental point is that other phenomena could be described by our modeling framework, which is formulated in a generic d dimension: the key idea is to choose the phenomenon and experimental setting under investigation, and, once they are fixed, then the appropriate modeling choice of dimension d and of the microscopic mechanism and model can be done. In particular, the approach (2.6) gives a higher possibility of describing the details of the microscopic mechanisms, instead of imposing the appropriate average taken from experimental results, as done here using the microscopic rule (2.7). For instance, our main goals in the near future are the modeling of an independent sensing of multiple directional cues and the modeling of the biphasic response of the cells to the ECM. Ongoing projects directly implementable within the present framework include the description of a time-varying ECM, because of remodeling, through the introduction of appropriate microscopic rules for the dynamics of the fibers' direction.

REFERENCES

[1] V. CALVEZ, G. RAOUL, AND C. SCHMEISER, *Confinement by biased velocity jumps: Aggregation of escherichia coli*, Kinet. Relat. Models, 8 (2015), pp. 651–666.

[2] S. CAREY, Z. GOLDBLATT, K. MARTIN, B. ROMERO, R. WILLIAMS, AND C. REINHART-KING, *Local extracellular matrix alignment directs cellular protrusion dynamics and migration through Rac1 and FAK*, Integr. Biol., 8 (2016), pp. 821–835.

[3] F. A. C. C. CHALUB, P. A. MARKOWICH, B. PERTHAME, AND C. SCHMEISER, *Kinetic models for chemotaxis and their drift-diffusion limits*, Monatsh. Math., 142 (2004), pp. 123–141.

[4] G. CHARRAS AND E. SAHAI, *Physical influences of the extracellular environment on cell migration*, Nat. Rev. Mol. Cell Biol., 15 (2014), pp. 813–824.

[5] A. CHAUVIERE, T. HILLEN, AND L. PREZIOSI, *Modeling cell movement in anisotropic and heterogeneous network tissues*, Netw. Heterog. Media, 2 (2007), pp. 333–351.

[6] A. CHAUVIERE, T. HILLEN, AND L. PREZIOSI, *Modeling the motion of a cell population in the extracellular matrix*, Discrete Contin. Dyn. Syst., 2007 (2007), pp. 250–259.

[7] F. A. CHIARELLO AND A. TOSIN, *Macroscopic limits of non-local kinetic descriptions of vehicular traffic*, Kinet. Relat. Models, 16 (2023), pp. 540–564.

[8] M. CONDOR, C. MARK, R. GERUM, N. GRUMMEL, A. BAUER, J. M. GARCIA AZNAR, AND B. FABRY, *Breast cancer cells adapt contractile forces to overcome steric hindrance*, Biophys. J., 116 (2019), pp. P1305–P1312, https://doi.org/10.1016/j.bpj.2019.02.029.

[9] M. CONTE AND N. LOY, *Multi-cue kinetic model with non-local sensing for cell migration on a fibers network with chemotaxis*, Bull. Math. Biol., 84 (2022), 42.

[10] R. B. DICKINSON, *A generalized transport model for biased cell migration in an anisotropic environment*, J. Math. Biol., 40 (2000), pp. 97–135.

[11] F. FILBET, P. LAURENCOT, AND B. PERTHAME, *Derivation of hyperbolic models for chemosensitive movement*, J. Math. Biol., 50 (2005), pp. 189–207.

[12] F. FILBET AND C. YANG, *Numerical simulation of kinetic models for chemotaxis*, SIAM J. Sci. Comput., 36 (2014), pp. B348–B366, https://doi.org/10.1137/130910208.

[13] M. FORNASIER, J. HASKOVEC, AND G. TOSCANI, *Fluid dynamic description of flocking via Povzner–Boltzmann equation,* Phys. D, 240 (2010), pp. 21–31, https://doi.org/10.1016/j.physd.2010.08.003.

[14] P. FRIEDL, *Prespecification and plasticity: Shifting mechanisms of cell migration*, Curr. Opin. Cell Biol., 16 (2004), pp. 14–23.

[15] P. FRIEDL AND E.-B. BROCKER, *The biology of cell locomotion within three dimensional extracellular matrix*, Cell. Mol. Life Sci., 57 (2000), pp. 41–64.

[16] A. GHAFFARIZADEH, R. HEILAND, S. FRIEDMAN, S. MUMENTHALER, AND P. MACKLIN, *PhysiCell: An open source physics-based cell simulator for 3-D multicellular systems*, PLoS Comput. Biol., 14 (2018), e1005991.

[17] I. GONÇALVES AND J. GARCIA-AZNAR, *Extracellular matrix density regulates the formation of tumour spheroids through cell migration*, PLoS Comput. Biol., 17 (2021), e1008764.

[18] W. HAN, S. CHEN, W. YUAN, Q. FAN, J. TIAN, X. WANG, L. CHEN, X. ZHANG, W. WEI, R. LIU, J. QU, Y. JIAO, R. H. AUSTIN, AND L. LIU, *Oriented collagen fibers direct tumor cell intravasation*, Proc. Natl. Acad. Sci. USA, 113 (2016), pp. 11208–11213.

[19] T. HILLEN, *M5 mesoscopic and macroscopic models for mesenchymal motion*, J. Math. Biol., 53 (2006), pp. 585–616.

[20] T. HILLEN AND H. G. OTHMER, *The diffusion limit of transport equations derived from velocity-jump processes*, SIAM J. Appl. Math., 61 (2000), pp. 751–775, https://doi.org/10.1137/S0036139999358167.

[21] M. LACHOWICZ AND M. PULVIRENTI, *A stochastic system of particles modelling the euler equations*, Arch. Ration. Mech. Anal., 109 (1990), pp. 81–93.

[22] J. R. LANGE AND B. FABRY, *Cell and tissue mechanics in cell migration*, Exp. Cell Res., 319 (2013), pp. 2418–2423.

[23] R. LEVEQUE, *Finite Difference Methods for Ordinary and Partial Differential Equations: Steady-State and Time-Dependent Problems*, SIAM, Philadelphia, 2007, https://doi.org/10.1137/1.9780898717839.

[24] N. LOY, T. HILLEN, AND K. PAINTER, *Direction-dependent turning leads to anisotropic diffusion and persistence*, European J. Appl. Math., 33 (2022), pp. 729–765.

[25] N. LOY AND L. PREZIOSI, *Kinetic models with non-local sensing determining cell polarization and speed according to independent cues*, J. Math. Biol., 80 (2020), pp. 373–421.

[26] N. LOY AND L. PREZIOSI, *Modelling physical limits of migration by a kinetic model with nonlocal sensing*, J. Math. Biol., 80 (2020), pp. 1759–1801.

[27] N. LOY AND L. PREZIOSI, *Stability of a non-local kinetic model for cell migration with density dependent orientation bias*, Kinet. Relat. Models, 13 (2020), pp. 1007–1027.

[28] N. LOY AND A. TOSIN, *Boltzmann-type equations for multi-agent systems with label switching*, Kinet. Relat. Models, 14 (2021), pp. 867–894.

[29] K. H. NAM, P. KIM, D. K. WOOD, S. KWON, D. H. PROVENZANO, AND P. PAND KIM, *Multiscale cues drive collective cell migration*, Sci. Rep., 6 (2016), 29749.

[30] H. OTHMER AND T. HILLEN, *The diffusion limit of transport equations II: Chemotaxis equations*, SIAM J. Appl. Math., 62 (2002), pp. 1222–1250, https://doi.org/10.1137/S0036139900382772.

[31] H. G. OTHMER, S. R. DUNBAR, AND W. ALT, *Models of dispersal in biological systems*, J. Math. Biol., 26 (1988), pp. 263–298.

[32] K. J. PAINTER, *Modelling cell migration strategies in the extracellular matrix*, J. Math. Biol., 58 (2008), pp. 511–543.

[33] L. PARESCHI AND G. TOSCANI, *Interacting Multiagent Systems: Kinetic Equations and Monte Carlo Methods*, Oxford University Press, Oxford, UK, 2013.

[34] J. PLOU, Y. JUSTE-LANAS, V. OLIVARES, C. DEL AMO, C. BORAU, AND J. GARCIA-AZNAR, *From individual to collective 3d cancer dissemination: Roles of collagen concentration and TGF-β*, Sci. Rep., 8 (2018), 12723.

[35] A. POVZNER, *The Boltzmann equation in kinetic theory of gases*, Amer. Math. Soc. Trans., 2 (1962), pp. 193–216.

[36] L. PREZIOSI AND M. SCIANNA, *Multi-level mathematical models for cell migration in confined environments*, in Methods of Mathematical Oncology, T. Suzuki, C. Poignard, M. Chaplain, and V. Quaranta, eds., Springer, Singapore, 2021.

[37] L. PREZIOSI AND G. VITALE, *Mechanics of tumor growth: Multiphase models, adhesion, and evolving configurations*, in New Trends in the Physics and Mechanics of Biological Systems, Lecture Notes of the Les Houches Summer School, Vol. 92, Oxford University Press, Oxford, UK, 2011, pp. 177–226.

[38] P. PROVENZANO, K. ELICEIR, J. CAMPBELL, D. INMAN, J. WHITE, AND P. KEELY, *Collagen re-organization at the tumor-stromal interface facilitates local invasion*, BMC Med., 4 (2006), pp. 1–15.

[39] P. PROVENZANO, K. ELICEIRI, AND P. KEELY, *Shining new light on 3d cell motility and the metastatic process*, Trends Cell Biol., 19 (2009), pp. 638–648.

[40] P. PROVENZANO, D. INMAN, K. ELICEIRI, J. KNITTEL, L. YAN, C. RUEDEN, J. WHITE, AND P. KEELY, *Collagen density promotes mammary tumor initiation and progression*, BMC Med., 6 (2008), pp. 1–15.

[41] A. QUARTERONI AND A. VALLI, *Numerical Approximation of Partial Differential Equations*, Springer Ser. Comput. Math. 23, Springer-Verlag, Berlin, 2008.

[42] A. RAY, R. MORFORD, N. GHADERI, D. ODDE, AND P. PROVENZANO, *Dynamics of 3d carcinoma cell invasion into aligned collagen*, Integr. Biol., 10 (2018), pp. 100–112.

[43] A. RAY, Z. SLAMA, R. MORFORD, S. MADDEN, AND P. PROVENZANO, *Enhanced directional migration of cancer stem cells in 3d aligned collagen matrices*, Biophys. J., 112 (2017), pp. 1023–1036.

[44] T. RISTORI, T. NOTERMANS, J. FOOLEN, N. KURNVIAWAN, C. BOUTEN, F. BAAIJENS, AND S. LOERAKKER, *Modelling the combined effects of collagen and cyclic strain on cellular orientation in collagenous tissues*, Sci. Rep., 8 (2018), 8518.

[45] J. SAPUDOM, S. RUBNER, S. MARTIN, AND T. POMPE, *Mimicking tissue boundaries by sharp multiparameter matrix interfaces*, Adv. Healthc. Mater., 5 (2016), pp. 1861–1867.

[46] M. SCIANNA AND L. PREZIOSI, *Modeling the influence of nucleus elasticity on cell invasion in fiber networks and microchannels*, J. Theor. Biol., 317 (2013), pp. 394–406.

[47] M. SCIANNA, L. PREZIOSI, AND K. WOLF, *A cellular Potts model simulating cell migration on and in matrix environments*, Math. Biosci. Eng., 10 (2013), pp. 235–261.

[48] D. W. STROOCK, *Some stochastic processes which arise from a model of the motion of a bacterium*, Z. Wahrscheinlichkeit, 28 (1974), pp. 305–315.

[49] P. TAUFALELE, J. VANDERBURGH, A. MUNOZ, M. ZANOTELLI, AND C. REINHART-KING, *Fiber alignment drives changes in architectural and mechanical features in collagen matrices*, PLoS One, 14 (2019), e0216537.

[50] J. TIEN, U. GHANI, Y. DANCE, A. SEIBEL, M. KARAKAN, K. EKINCI, AND C. NELSON, *Matrix pore size governs escape of human breast cancer cells from a microtumor to an empty cavity*, iScience, 23 (2020), 101673.

[51] K. WOLF, M. TE LINDERT, M. KRAUSE, S. ALEXANDER, J. TE RIET, A. L. WILLIS, R. M. HOFFMAN, C. FIGDOR, S. J. WEISS, AND P. FRIEDL, *Physical limits of cell migration: Control by ECM space and nuclear deformation and tuning by proteolysis and traction force*, J. Cell Biol., 201 (2013), pp. 1069–1084.

[52] M. H. ZAMAN, L. M. TRAPANI, A. L. SIEMINSKI, D. MACKELLAR, H. GONG, R. D. KAMM, A. WELLS, D. A. LAUFFENBURGER, AND P. MATSUDAIRA, *Migration of tumor cells in 3d matrices is governed by matrix stiffness along with cell-matrix adhesion and proteolysis*, Proc. Natl. Acad. Sci. USA, 103 (2006), pp. 10889–10894.